Interdisciplinary project : Telescope performances, satellite track model and orbit simulations

Luca Hartman; Luc Luigi Guyot et Julien Thierry Burri

1   Introduction

Currently, the number of satellites orbiting in space is around 6500. When considering space debris, the total number of objects rises to 300'000'000. Among these debris, 30'000 are larger than 10 cm. The number of satellites is expected to increase eight times by 2030 [1]. Indeed, the space occupation is a worsening problem. The first step to tackle this challenge is to detect the objects, mainly using an optical observations. This report summarises the work done to provide a basis for the utilisation of the telescope and the processing of images taken by the Space Situational Awareness (SSA) *École Polytechnique Fédérale de Lausanne* (EPFL) association. Among these efforts, the Point Spread Function (PSF) was measured after taking into account the different optical aberrations. Satellite tracks have been modelled. Then, the influence of the environment has been quantified. Several perturbations have been studied such as light pollution between two locations and the clarity of the sky. Finally, the trajectory of satellites has been computed numerically. The convergence study of two different algorithms, Runge-Kutta 4 and Störmer-Verlet, has been made. The influence of several forces on the satellite has been studied.

2   Telescope

The detection of satellites and space debris can be done using two frequency bands: radio frequencies and visible light. In the SSA EPFL association, visible light has been selected as the first design. The prototype, called *LOST* (Low Orbit Satellite Tracker), consists of a telescope, a camera and a motorised mount. These elements have been selected based on specific requirements, notably limiting magnitude and angular resolution. This telescope's performances are to be measured in this project. The characteristics of the telescope, the camera and the mount are given in the Appendix A.

2.1   Experimental method

The measurements were taken during several nights at two different locations. The first one is on the EPFL campus and the second one is located at Astroval in the *Vallée de Joux*. The experimental setup, which is composed of the telescope, the camera, and the mount, is shown on Figure 16 in the Appendix A. The mount must be calibrated so that it can locate itself in space, point to the stars chosen by the operator and counter the rotation of the earth. The first step consists to target Polaris with a polar finder (optical scope) in order to angle the mount. Then a multitude of stars are aimed at and focused in the centre of the camera. Once 4-7 stars have been centred, the telescope is precisely calibrated. Then, the focus is finely tuned. The camera is cooled to -10 °C. Pictures of stars at different altitudes have been taken. Pictures of the same star were also taken with different exposure times. Theses photographs have been taken to find the limiting magnitude and the mean Full Width Half Maximum (FWHM). Pictures of satellites track were also taken to verify the accuracy of the track model.

3 Calibration

There are multiple sources of imprecision in the images taken with a telescope and a CMOS camera. Some are related to the sensor while others are related to the optical imperfections. For each effect, the source is presented, the effect measured and a solution to remove (or dampen) the effect is presented. While thermal noise would be considerable in normal astronomy images, the short exposure time (less than 1 s) implies there is no significant thermal noise. This exposure time is necessary to capture the satellite track with the end and beginning inside the image. Indeed, orbital determination need precise angles, which can not be provided if the track crosses the whole frame. Therefore, this source of noise will not be discussed in this chapter.

The quality of the optics can change across the sensor of the camera, with usually small angular resolution on the borders. This has been measured and is presented in the Appendix B.3.

3.1 Readout noise

In a CMOS camera sensor, a small charge is generated when a photon hits a pixel. This small charge is converted into a voltage using an amplifier. The voltage of all the pixels in the column are then transferred to the sides of the sensor. At this point, the analogue signal is converted into a digital signal, which is recorded on the computer [2].

The amplifier and analogue-digital converter are the noise sources. Since each pixel has its amplifier, there can be a different noise value for each pixel. This gives rise to a noise distribution that is independent of the exposure time, unlike the thermal noise. Because of this, it can easily be measured by taking a picture with the shortest exposure time possible; the short time measurement does not allow the other effects to impact the image. For the camera used, the minimal exposure time on the camera is 1 ms.

Because this noise is statistical in nature, averaging it over multiple images will give more representative results. The average image, called *master bias frame*, can then be used to calibrate the image. This image's

Figure 1: Readout noise histogram with Gaussian fit at sensor temperature $T = -10$ °C. The camera is set to low gain and an exposure time of 1 ms.

histogram is shown on Figure 1. Visibly, the distribution is a narrow Gaussian; this is confirmed by the Gaussian fit's good agreement with the data and its small standard deviation of $\sigma = 1$. This explains why this effect is called a *bias*, as it effectively a uniform shift of 500 in luminosity across the whole image.

To dampen this effect, the master bias frame is subtracted from all the images. The master bias frame is also subtracted from the other calibration frames. An example for the difference this calibration produces is shown in the Appendix B.1 on Figure 17a on Figure 17b.

3.2 Uneven luminosity and parasite reflections

The whole sensor map would, in the case of a perfect telescope, receive the same light flux. In reality, this is not the case, as the flux is at its maximum at the centre and decreases further
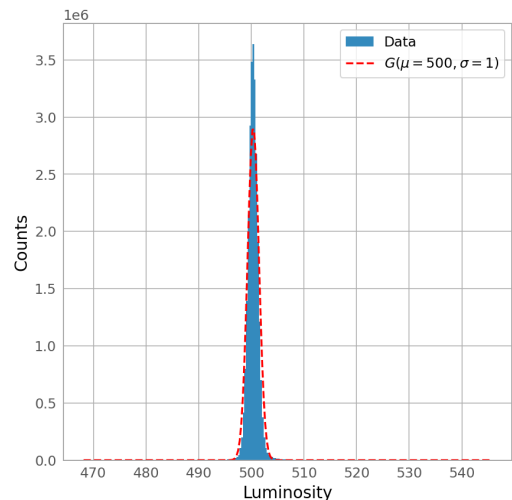
out. A round symmetry of the telescope is expected in this effect, even though the camera sensor is rectangular.

The internal reflections can lead to parasite lights. This effect is especially present in highly complex telescopes with large secondary mirrors suspended by multiple movable arms. An example from the *VST* is shown in the Appendix B.2.

In order to remove the variation in luminosity and the parasite lights, the telescope operator can take multiple pictures of a uniformly luminous area. Usually, this is done by taking an image of the sky during the time between the sunset and the apparition of the first stars. Any change in light flux across the camera sensor will be present and thus measurable. Such images are called *flat frames*; usually, the flat frame used for calibration is the average of multiple flat frames [3].

In order to dampen this effect, the image is normalised such that the average value across the whole image is 1. This is necessary to preserve the luminosity of the objects. Furthermore, the correction is not in absolute luminosity, but in relative luminosity between different areas of the camera sensor. The raw image (normalised) is shown on Figure 2a and the obtained image is shown on Figure 2b. The second image is obtained by dividing each pixel of the raw image by the value of the corresponding pixel in the flat frame.
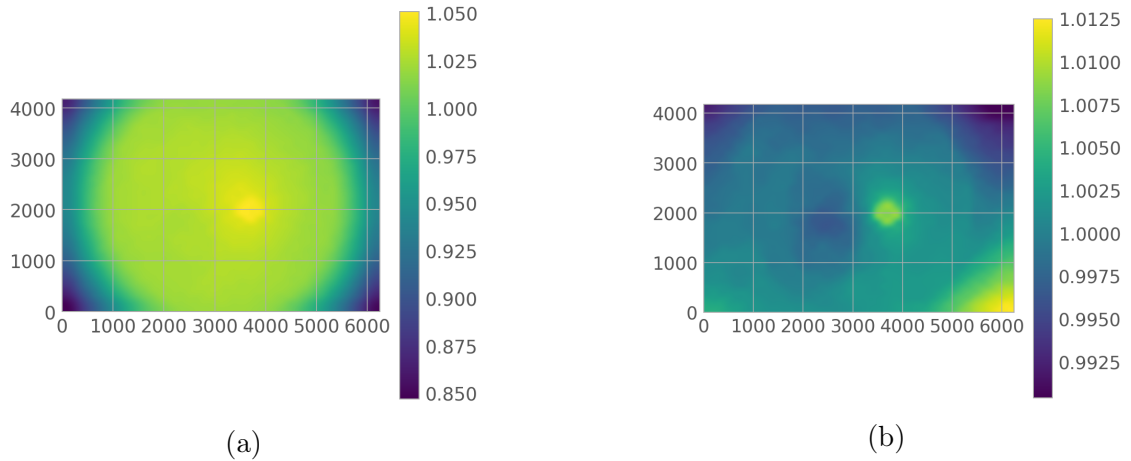

(a) (b)

Figure 2: Variation in background brightness for the raw image (a) and the calibrated image (b). For easier comparison, both images have been normalised so that the mean value is 1.

4 Track extraction

Figure 3: Example of a satellite track. In this image, the satellite in question is a Starlink satellite from the company SpaceX. The expo-sure time is 0.5 s.

The purpose of the LOST prototype is to detect satellites and measure their characteristics. One example of a track is shown in Figure 3. To compute its orbit, three sets of precise angles are needed. Those angles are computed from the location of the beginning and end of the track relative to the centre of the image. The direction the telescope is pointing (i.e. the angular coordinates of the centre of the image) is known from the indications of the mount and the plate solving. Precise angles are needed to have precise orbit determination, and therefore the precise coor-

dinates of the beginning and end of the track are needed. This precision is hampered by the prototype's angular resolution.

Applying forward modelling techniques on the track, one can find the model best describing the recorded track. This allows for angle determinations smaller than the angular resolution. This model also gives more information, such as the brightness of the track and its width.

The algorithm used to find the best model is a version of the Monte-Carlo algorithm. Its aim is to maximise the log probability of a given set of parameter. The log probability depends on the model goodness, which is measured with the reduced chi-square test. The algorithm determines the best parameters as well as the confidence interval. Further details are presented in Chapter C in the Appendices.

4.1 Point Spread Function

The limit in angular resolution is measured by the PSF. This is the light emitted by a point source captured by the camera sensor after it has gone through the atmosphere and the optics. In practice, any star can be considered a point source, and thus the PSF can be computed based on any star in the image[1]. An example of a star is shown in Figure 4a. Since the PSF can vary across the camera sensor, a star close to the track is used.

The imprecision caused by the atmosphere and the optics are generally expected to follow a Gaussian distribution. Since the PSF can be stretched along a direction (for example because of poor accuracy in the sky tracking), the Gaussian is of elliptical form defined by an angle θ. Its equation is given by

$$f(x,y) = A \exp\left(-\left(a(x-x_0)^2 + 2b(x-x_0)(y-y_0) + c(y-y_0)^2\right)\right), \tag{1}$$

where A is the amplitude, (x_0, y_0) is the coordinates of the maximum and

$$a = \frac{\cos^2\theta}{2\sigma_x^2} + \frac{\sin^2\theta}{2\sigma_y^2},$$

$$b = -\frac{\sin 2\theta}{4\sigma_x^2} + \frac{\sin 2\theta}{4\sigma_y^2},$$

$$c = \frac{\sin^2\theta}{2\sigma_x^2} + \frac{\cos^2\theta}{2\sigma_y^2},$$

with σ_x and σ_y the standard deviation along the x and y axis. A Gaussian fit on the PSF is done to extract the FWHM. This value is generally considered to be the maximal angular resolution. Such a fit is shown in Figure 4b.

The camera sensor can be describe by a discretized plane with coordinates (x, y). A light flux can then be mathematically described as a field $f(x, y)$ defined on the plane of the camera sensor (where x and y are the horizontal and vertical coordinates in in the image). Similarly, the PSF can be described as a field $h(x, y)$. In this case, the capture image will be given by the field defined by

$$g(x,y) = (f * h)(x,y) = \sum_{(x',y') \in \text{ sensor}} f(x,y)h(x-x', y-y'). \tag{2}$$

---

[1]One has to take care not to use a saturated star. Such a star appears as a large blob in the image, even though its angular diameter is much smaller than the angular resolution of the optical instrument. In this case, the PSF will be very large.
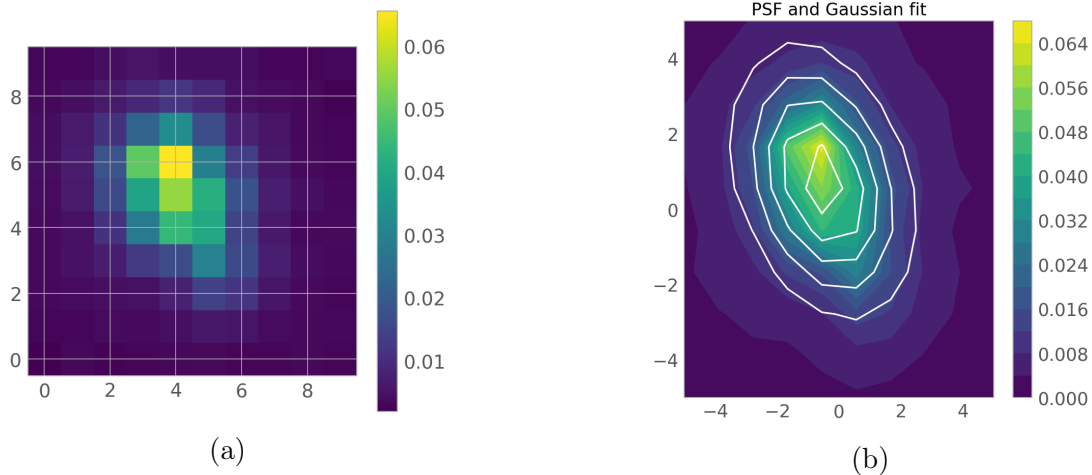
Figure 4: Point spread function obtained from a star (a) and its associated 2D Gaussian best fit (b).

Typically, the PSF is defined on a smaller part of the image, only enough to fully contain the star. In this report, the image outcut has been consistently 10×10 pixels. In this case, the sum is done on this outcut instead of the whole sensor. This vastly increases performances for a small precision cost [4].

4.2 Track model

The track model developed during this project has been relatively simple. The light flux reflected by the satellite or space debris is considered to be constant in time and uniform across the whole object. This model is therefore defined by 6 parameters: the coordinates of the beginning and end of the tracks (i_0, j_0) and (i_{end}, j_{end}), the width w and the amplitude A. An example is shown on Figure 5a. In this case, the parameters are described by $\theta = (i_0, i_{end}, w, A)$.

This track model is then convolved using the measured PSF to simulate what the prototype would have captured. The result obtained using the track model shown in Figure 5a and the PSF shown on Figure 4a is presented on Figure 5b.

To decrease computation time, a simplified model has been used. This model assumes the track begins and ends beyond the outcut of the image. This effectively sets the parameters $j_0 = 0$ and $j_{end} = $ length of outcut.

4.3 Real track

Since the forward modelling is capable of finding the correct parameters based on a fake track, the next step was to apply this algorithm to a real track. Multiple tracks were studied, but only one case is shown here. The outcut of the image containing the track is shown on Figure 6a. The difference between the data and the best model is shown on Figure 6b. The best parameters were $\theta = (i_0 = 500, j_0 = 68, i_{end} = 41, j_{end} = 672, w = 8, A = 650)$. The reduced chi-square test for the best model gives $\chi^2_{red} = 17$. The optimal parameters given by the Monte-Carlo simulation are identical to the initial parameters.

The trajectories of the 400 walkers[2] are shown on Figure 7a and the corner plot[3] is shown on Figure 7b. The number of iteration is 10^5.

---

[2]The term *walkers* is defined in the Appendix C.

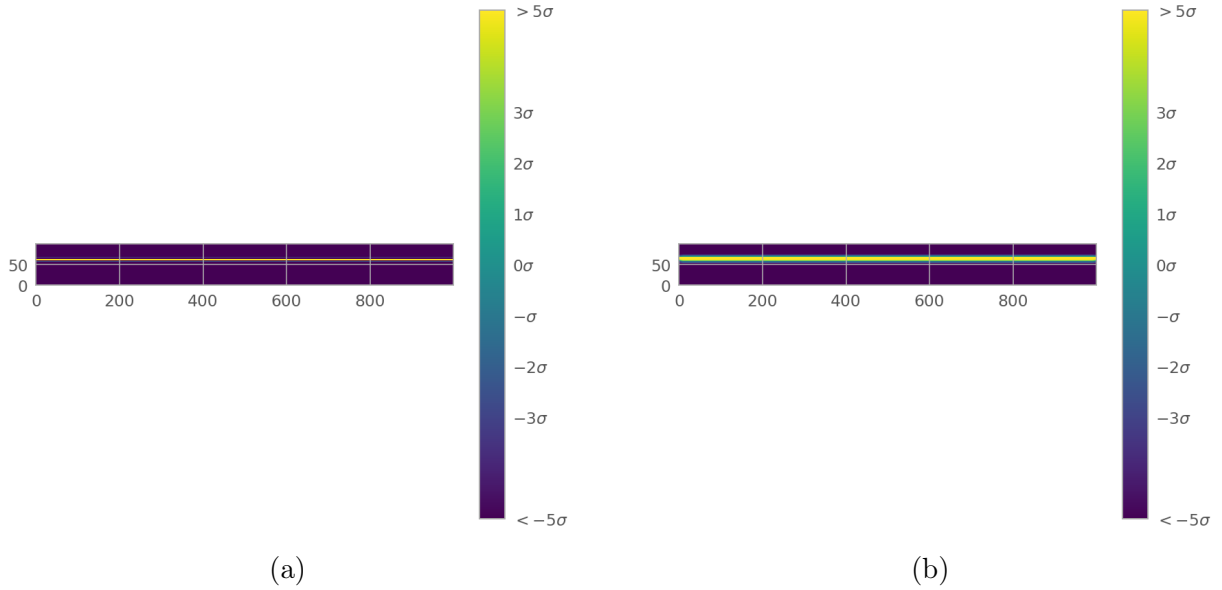[3]The term *corner plot* is defined in the Appendix C.

5

Figure 5: An example of a track model (a) and the result after convolution with the PSF (b). The track model's parameters were $i_0 = 60$, $j_0 = 0$, $i_{end} = 30$, $j_{end} = 1000$, $w = 1$ and $A = 1000$.
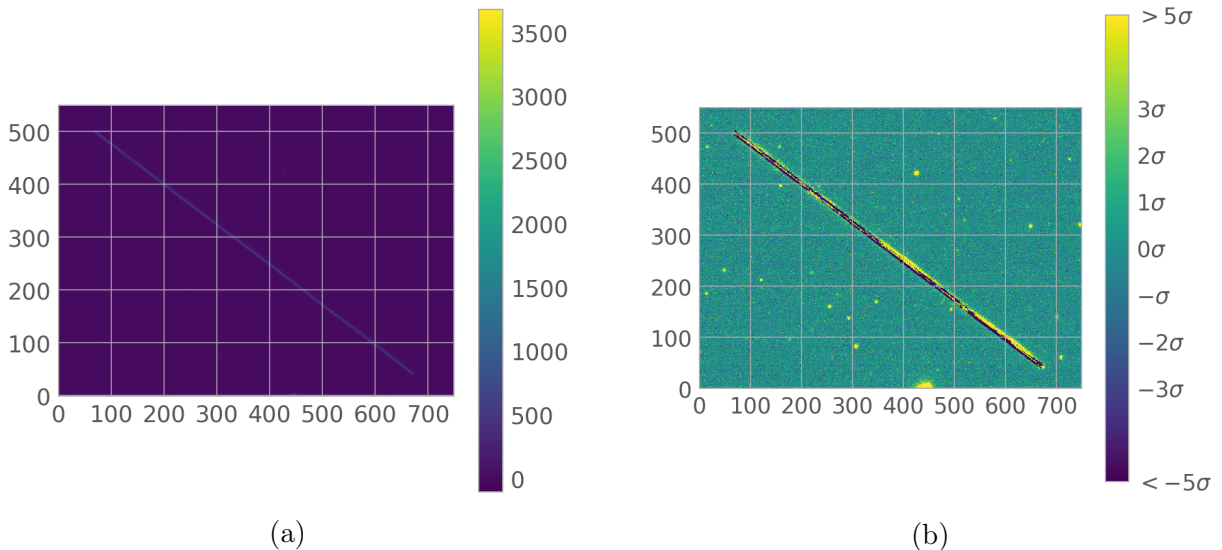

Figure 6: Outcut of an image showing a real track (a) and the difference bewteen the real track and the best model (b). The SNR is 288. The reduced chi-square test gives $\chi^2_{red} = 17$. The parameters were $\theta = (i_0 = 500, j_0 = 68, i_{end} = 41, j_{end} = 672, w = 8, A = 650)$.
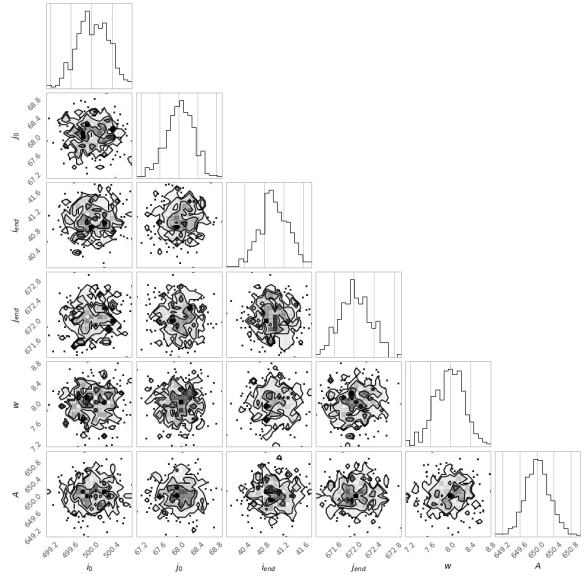
4.4 Low SNR

In order to quantify how bright the track is compared to the background, the signal to noise ratio (SNR) is computed. The background noise follows a Poisson distribution, whose mean value is μ. The SNR is then given by the equation

$$\text{SNR} = A/\mu. \tag{3}$$

The background noise distribution with its Poisson fit and the solution found by the Monte-Carlo simulation (with its associated confidence interval) is shown in Figure 8a. The lower limit for proper convergent results has been found to be an amplitude of 1000 for a background noise with mean value 62; this represents a SNR of 16. An example of the corner plot obtained
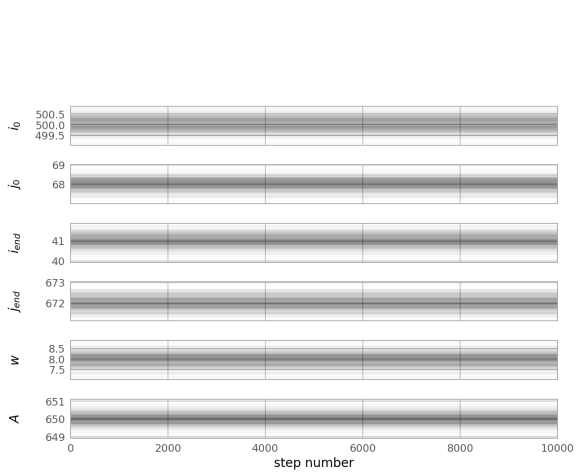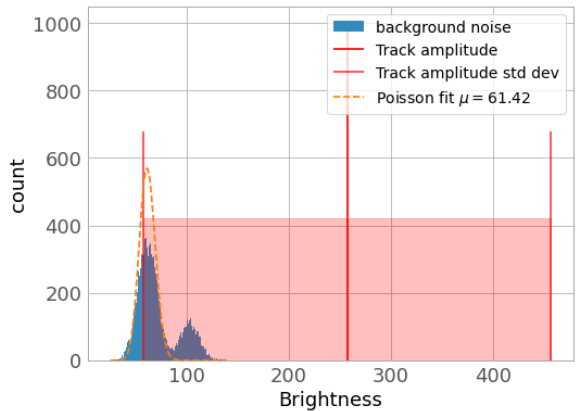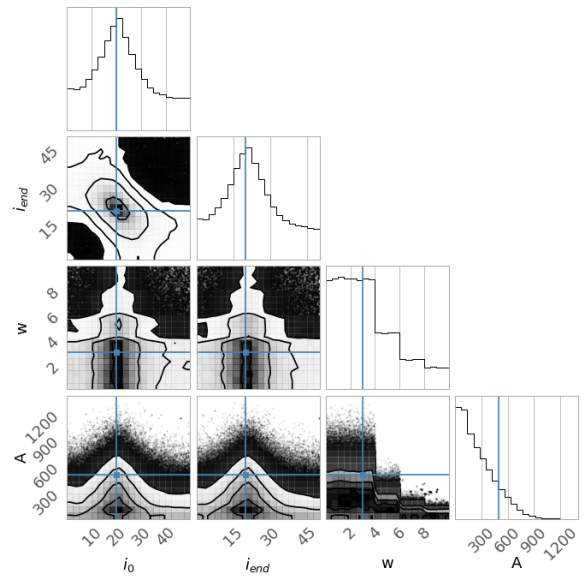
Figure 7: Walkers (a) and corner plot (b) for a Monte-Carlo simulation for a real track. The SNR is 288. The figures are a qualitative representation of the behaviour of the simulation.

after running the Monte-Carlo simulation for a low SNR is shown on Figure 8b. The associated background distribution and the solution for the amplitude is shown in Figure 8a.

Figure 8: The background distribution with the solution found using Monte-Carlo simulation (a) and the corner plot of the parameters (b). The real amplitude is $A = 500$, which gives a SNR of 8.

4.5 Over-sampling

Since the track width is usually very small (usually less than 10 pixels) and the width is treated as an integer, issues arise by the fact that real values between integers give the exact same

track. In order to avoid this, one solution is to increase the number of pixels in the image; this is over-sampling. In practice, this means replacing every pixel by f pixels in each direction, where f is the oversampling factor. For instance, a 4×4 image becomes a 8×8 image. This helps the algorithm to converge.

The drawback is the increase in computation time. Indeed, the biggest computational cost is the convolution of the track model with the PSF. The time complexity of a convolution between a track model with dimensions $N \times M$ and a PSF with dimensions $n \times m$ is $\mathcal{O}(NMnm)$, which thus scales as f^4 when over-sampled by a factor of f.

This technique has been tested on a fake track, in order to compare the solutions from the Monte-Carlo simulation to the true parameters. The track data, the track obtained from the parameters θ, and the PSF are over-sampled at each iteration. The behaviour of the walkers during the maximisation for a scaling factor $f = 2$ is shown in Figure 9a. The resulting parameter distributions are shown in Figure 9b. No higher scaling factors have been tested due to computational time constraints[4].
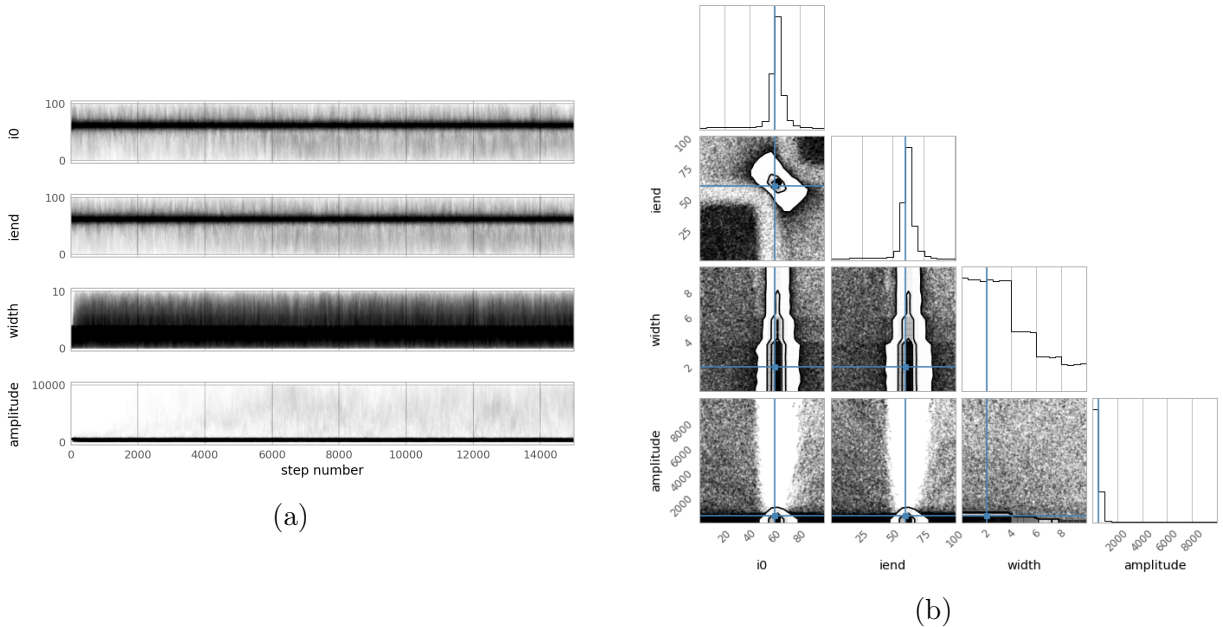

Figure 9: The trajectory of all walkers during the Monte-Carlo simulation (a) and the corner plot of the parameters (b). The blue lines represent the actual values. The outcut of the track and the PSF have been over-sampled with a factor of 2. The figures are a qualitative representation of the behaviour of the simulation.

5   Influence of the environment

5.1   Methods

The limiting magnitude is the magnitude of the faintest star in a picture. The analysis of theses images is made with the program *Astrometric Stacking program* (ASTAP). The detection limit is a signal-to-noise ratio bigger or equal to 7 [5]. The limiting magnitude is calculated over plenty of images and the mean value is taken. The error is the standard deviation. In order to

---

[4]The computation for the same track takes about 20 minutes without over-sampling, but 4 hours with an over-sampling by a factor of $f = 2$. Furthermore, more iterations are needed to achieve proper ensemble sampling, which increases the computational time to 10 hours. This comparison was done on a high-performance computer lent by the eSpace centre at EPFL.

Time	0.02 s	0.5 s	1 s	5 s	30 s	60 s	180s
Astroval	10.7 ± 0.2	-	13.3 ± 0.1	14.3 ± 0.1	15.0 ± 0.2	-	-
Campus	not detect.	13.3 ± 0.1	13.6 ± 0.1	14.4 ± 0.1	15 ± 0.1	15.5 ± 0.2	16.4 ± 0.5

Table 1: Magnitude of the faintest star observable at Astroval and on the campus as a function of exposure time.

calculate the FWHM, stars were fitted with a 2D-Gaussian. These stars are those that have not saturated the sensor. The mean is taken over all these stars. The error is the standard deviation.

5.2 Results

First, it was observed that too few stars were detected when measurements were taken at 7 degrees altitude during an exposure time of 0.02 s on the EPFL campus. This is not the case when this measurement is taken at Astroval. Table 1 shows the magnitude of the faintest star observable with the telescope as a function of the exposure time. It can be observed that the longer the time exposure, the bigger the limiting magnitude. Figure 10a and Figure 10b show the full width at half maximum of the 2D-Gaussian point spread function. Theses sets of measurements were taken during two different nights at Astroval for time exposure of 0.5 s and 10 s. The results obtained on the EPFL campus is shown in Appendix F. Using another technique proposed by Prof. Kneib, others results have been obtained. They are shown in Appendix F. The technique takes into account only stars that have a SNR sufficiently small $SNR < 100$.
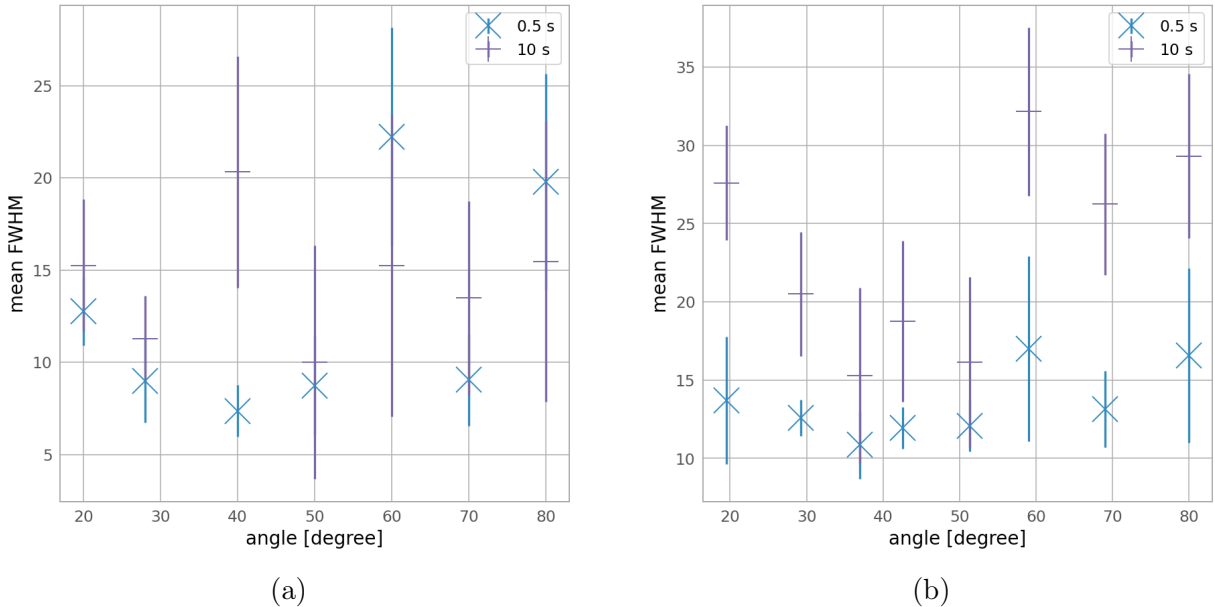

Figure 10: FWHM at astroval the first night (a) and second night (b) as a function of the altitude.

5.2.1 Light pollution

Figure 11a and Figure 11b show the magnitude of the faintest star that can be seen in a picture as a function of the telescope's target altitude. One set of measurements was taken on the

campus where the light pollution of cities like Lausanne or Evian is significant. The other set was taken at Astroval, on the top of a plateau in the Jura mountain chain, where there is almost no light pollution. The measurement taken at 72 degree in Figure 11b should not be taken into account. Indeed, this data has been corrupted by wind. The wind tends to make the telescope's tube vibrate. Therefore, the picture taken are slightly blurry. A tendency emerges, the larger the viewing angle, the higher the limiting magnitude. The magnitude of the faintest star observable on the EPFL campus tends to be smaller than the one at Astroval no matter how long the exposure time is.
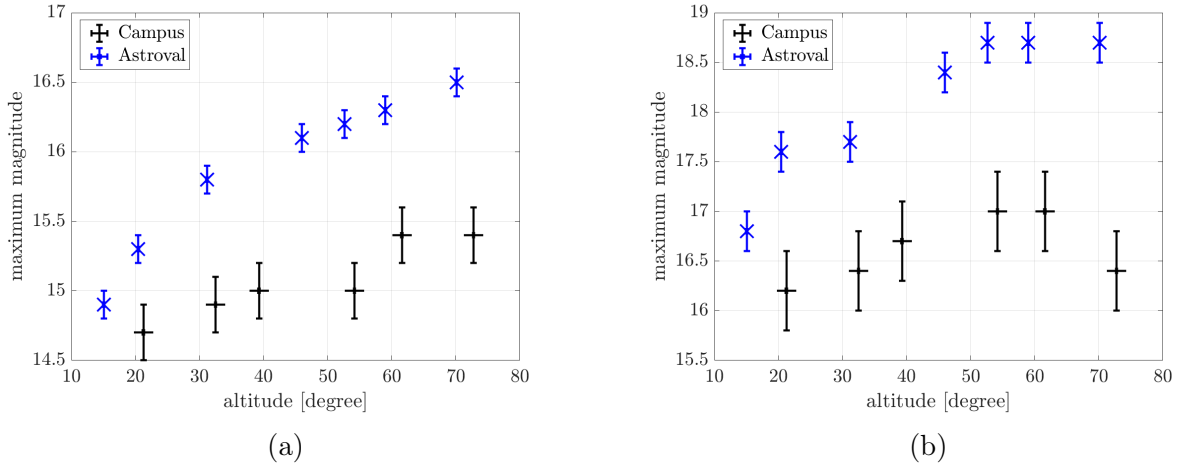

Figure 11: Maximum magnitude of stars observed from Astroval and from the EPFL campus. The exposure time is 0.5 s for Figure (a) and 10 s for (b).

5.2.2 Sky clarity

Figure 12a and Figure 12b show the magnitude of the faintest star detectable by the telescope. The measurements were taken at Astroval with time exposure of 0.5 s and 10 s. One set of data was taken during a night when the sky wasn't clear with some scattered clouds.
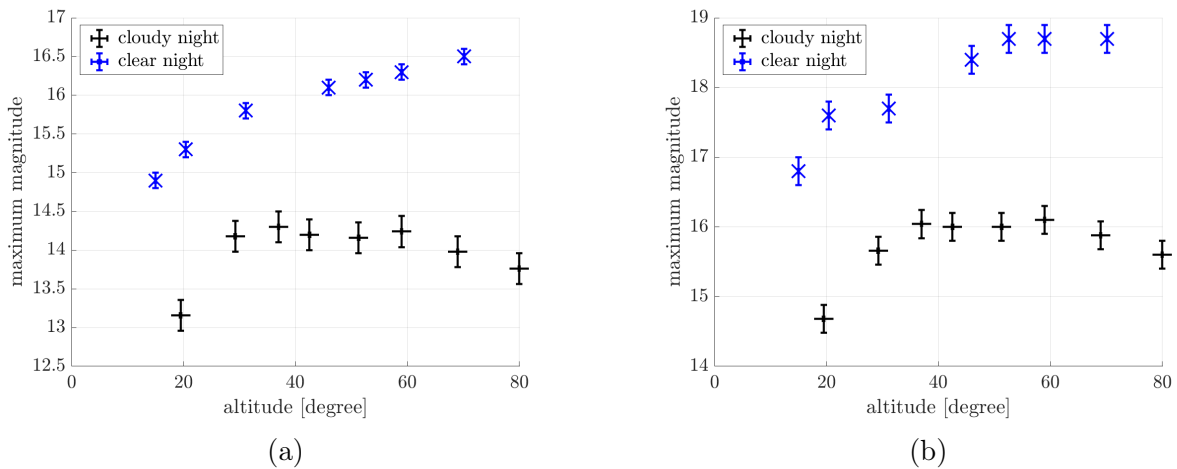

Figure 12: Maximum magnitude of stars observed from Astroval. The exposure time is 0.5 s for Figure (a) and 10 s for (b). One set of data were taken with a clear sky. The other one were taken with some clouds.

5.2.3 Temperature and wind

Figure 13a and Figure 13b show the limiting magnitude of stars observed during two different nights on the EPFL campus. During both nights, the atmospheric pressure was (996 ± 5) hPa and the humidity rate was $(54 \pm 2)\%$. The main difference was the temperature and the wind. As already mentioned in the section 5.2.1, the data taken at 72 degree should be discarded because of the significant influence of wind.
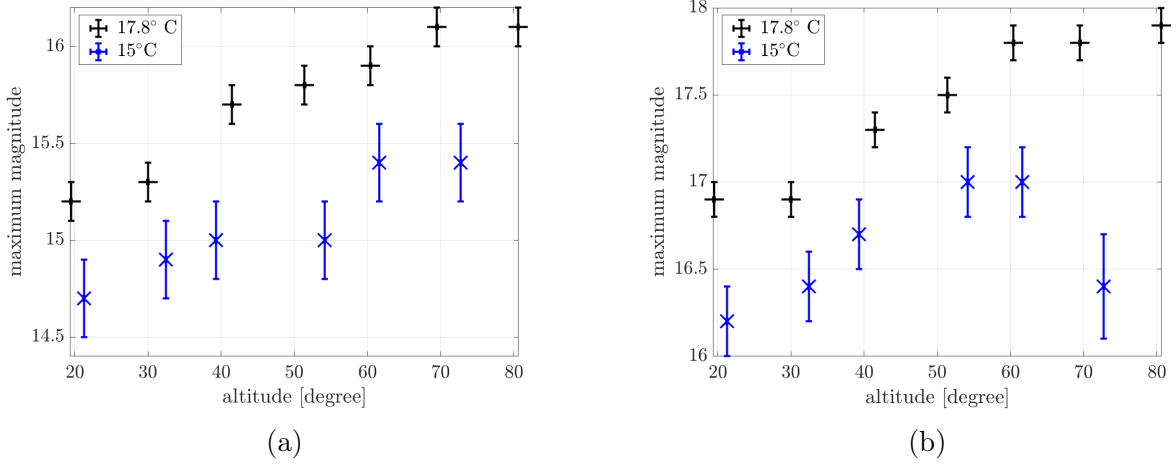

(a)

(b)

Figure 13: Maximum magnitude of stars observed from the EPFL campus. The exposure time is 0.5 s for Figure (a) and 10 s for (b). The atmospheric pressure and the humidity rate were approximately the same at (996 ± 5) hPa and 54% for both measurements [6].

6 Simulations

A C++ code has been implemented to predict the trajectory of satellites that have been detected by LOST. After the detection, an approximate orbit can be calculated. It doesn't take into account some external forces. Consequently, this simulation is required to predict long-term orbit. In order to compute the evolution of the satellite's position and velocity, the algorithms of Runge-Kutta 4 and Störmer-Verlet are used to integrate numerically the movement equation. The details of the implementation are given in Appendix E.4.

6.1 Convergence study

Figure 14a and Figure 14b show the convergence study of both algorithms. The only force used during the convergence study is the gravitational force with the point like Earth. The error between the initial and last position is represented as a function of the number of steps. The time simulated is 5579.995 s. There exists a minimum around 240 steps in the Figure 14a. This minimum corresponds to a Δt of 4 minutes.

6.2 Forces considered

In Table 2 are listed the forces considered and their typical accelerations applied on a satellite.
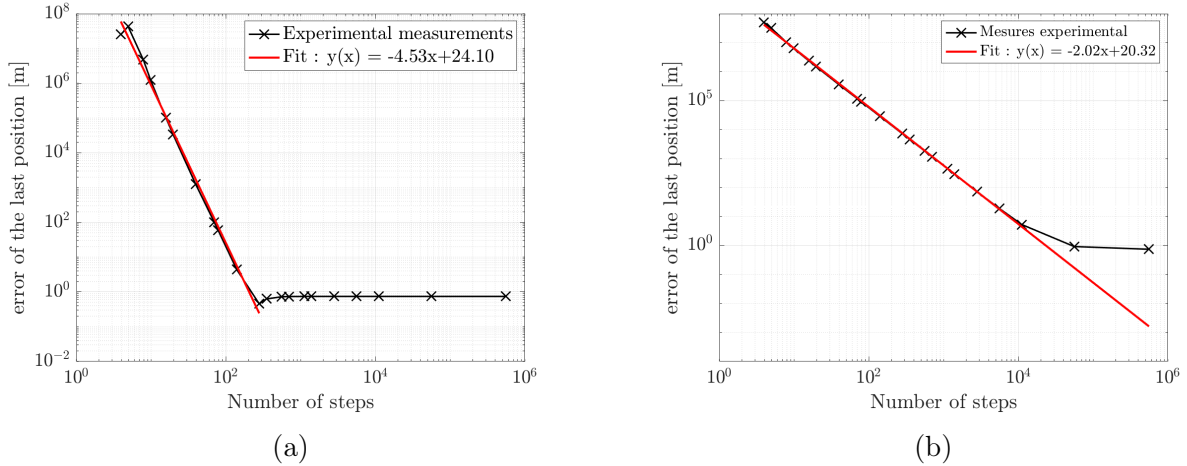
(a)   (b)

Figure 14: Convergence study of Runge-Kutta 4 (a) and of Störmer-Verlet (b) with a linear fit that did not take into account the values from the plateau. The convergence is made over the number of steps during 5579.995 s.

Type of Force	Acceleration at 400 km	Acceleration at 1000 km
Point like Earth Gravitation	8.7	7.3
Correction Due To 3D Earth	$1.3 \cdot 10^{-2}$	$8.9 \cdot 10^{-3}$
Atmospheric Drag Max	$2.3 \cdot 10^{-6}$	$6.0 \cdot 10^{-9}$
Moon's Gravitation	$1.2 \cdot 10^{-6}$	
Sun's Gravitation	$5.4 \cdot 10^{-7}$	
Atmospheric Drag Min	$5.3 \cdot 10^{-7}$	$2.9 \cdot 10^{-10}$
Solar Radiation Pressure	$4.5 \cdot 10^{-9}$	

Table 2: Typical values of the accelerations provoked by the different forces for altitudes of 400 km and 1000 km. For the Moon's gravitation, the Sun's gravitation and the solar radiation pressure the effects are considered equal for both altitudes since this variation is small compare to the Earth-Sun and Earth-Moon distances. The effects are listed by descending order for an altitude of 400 km. The computations are detailed in Appendix E.3.

6.3   Comparison with the ISS

In order to be able to evaluate the accuracy of the simulation, it is needed to have a reference object which can be used as a point of comparison. The ISS has been chosen since it is possible to find a lot of data on that satellite. Based on the positions and velocities of this object that are given online [7], it is possible to compare the altitudes as shown on Figures 15a and 15b. For the point-like Earth model, the simulated satellite tends to drop in altitude reaching a difference of altitude $\Delta r = 35$ km. For the 3D Earth model, the amplitude of the oscillation grows rapidly but the average seems to match the one of the ISS. However, the altitude at the end of the simulation is $r = 6200$ km, which is smaller than the Earth radius.

7   Discussion

Calibration   While applying the master bias frame does not completely remove the granularity of the image, the standard deviation of the background noise has decreased from $\sigma = 44$ (raw image) to $\sigma = 29$ (calibrated image). Furthermore, it gives an image with more accurate luminosity values. In particular, areas without light sources (i.e. the sky between stars) are
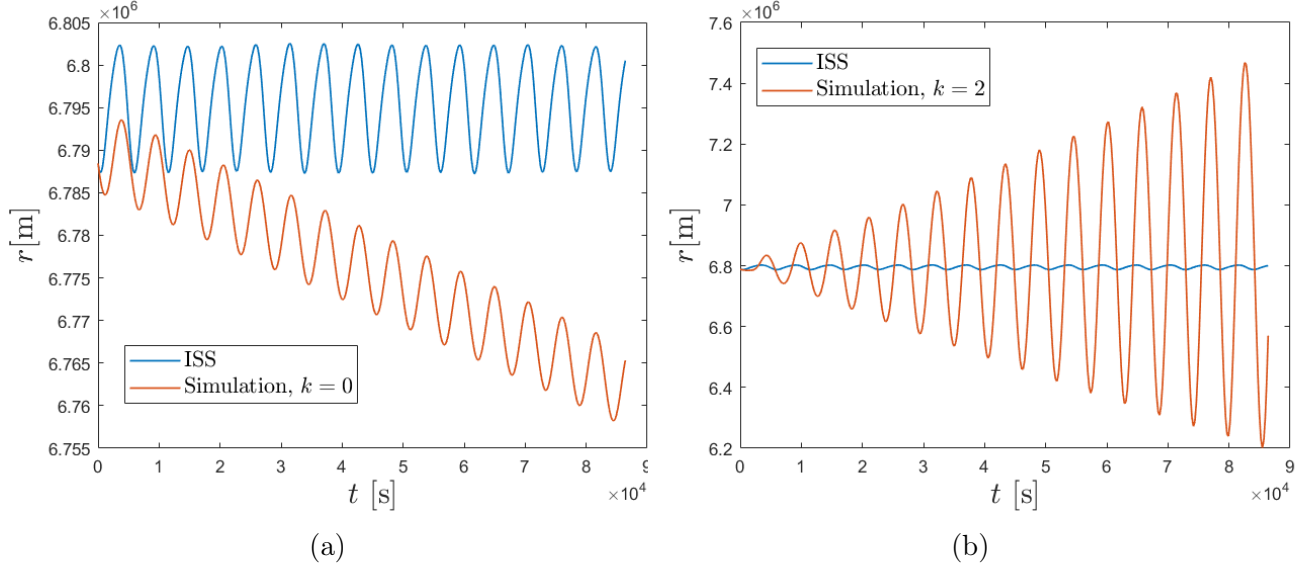
12

Figure 15: Comparison between the altitudes of the ISS and the simulated satellite. Two different orders of the geopotential, presented in Appendix E.2.2, are considered: $k = 0$ which corresponds to a point like mass Earth and $k = 2$ which corresponds to a 3D Earth model. The two altitudes are represented over a day.

almost completely black. The remaining luminosity is caused by the sky brightness. Indeed, the night sky has some intrinsic brightness, especially so when there is light pollution. Even after calibrating with the master flat frame, some relative changes in luminosity remain, although with smaller variations. Nonetheless, the variations in the calibrated image remain only in two corners and the largest part of the image is flat. It is worth pointing out that the bright spot around the coordinates $(4000, 2000)$ in Figure 2b is caused by the presence of a very bright star that completely saturated the camera sensor in this area. The methods used to extract the background values from images are sensible to such expanded bright spots.

Track extraction The Gaussian fit on the PSF shows great agreement, which confirms the assumption that the PSF can be approximated by Gaussian distribution. One can see that the introduction of an axis rotation is necessary to obtain proper results. The track model convolved with the PSF gives a result strongly reassembling real tracks, which confirms that the model is somewhat realistic.

The results obtained using the Monte-Carlo simulations are very promising when considering 4 parameters. Based on the behaviour of the walkers, the parameter space is properly explored in the vicinity of the solution. Few walkers wander further from the solution, which indicates a steep probability gradient around the solution. Furthermore, the difference between the reference (fake) track and the track obtained from the solution parameters is without the standard deviation of the background noise. The confidence interval on the coordinates of the beginning and end of the track are very small, which is needed for precise angle measurements.

The confidence interval is less than 1 pixel, which means that the simulations spends vastly more time on the correct value than next to it. For the width of the track, the confidence interval is 1 pixel, which means that tracks with wrong widths $(w \pm 1)$ are also relatively often explored by the walkers. This indicates that the effect of the width on the log likelihood is less than the effect of the coordinates. Because of this, precise width measurements are more complicated. As a reminder, 1 pixel represents an angle of 0.7", or 1.4 meter at 400 km. Finally, the confidence interval on the amplitude is also relatively small. This means there are hopes

to precisely measure the luminosity of the track.

When it comes to a real track, the Monte-Carlo simulations are not capable of finding any solution in a reasonable computational time. This is clearly visible in the image showing the difference between the real track and the best model. The behaviour of the walkers indicates there is very little chi-square gradient in the parameter space. This means that the walkers don't converge to the best solution. The small exploration is confirmed by the corner plot, which shows only a localised subspace of the parameter space. Multiple reasons could have been the cause of this.

The first is the impact of the relatively high noise on the real tracks. In order to test if this impacted the convergence of the walkers, tests based on a fake track (with known true parameters) have been conducted in order to find the limiting magnitude. While the results do suggest that problems arise when the SNR is low, the limit SNR found during the tests is significantly lower than that of the track. Therefore, the high noise will be a source of problems, but not in the particular cases studied in this project.

The second hypothesis is based on the poor handling of small track widths by the model. Over-sampling was implemented to dampen the effect of small widths. While better convergence has been found, it has been a the cost of exploding computational time. Since the track modelling should be done on every track detected during the night, the solution is not adapted. This technique remains usable for rare events. Furthermore, the tracks studied did not have tracks that were extremely small. For larger tracks, similar results were obtained with or without over-sampling. Therefore, this method is not expected to improve the results on real tracks.

Finally, the last hypothesis is on the impact of varying amplitude along the track. Indeed, small periodic variations (of about 10 % of the amplitude) has been observed on the tracks. This is much larger than the standard deviation of the background noise, which means this variation is significant. Since the model has a uniform amplitude, there is no possible amplitude that suits the measurements. At best, some parts of the track will be lighter than the model and other parts will be darker. Therefore, the chi-square test will always be relatively large. This means the log likelihood differences between two parameters will be small, and thus there is only a weak impetus for the walkers to explore the parameter space. Such a sinusoidal variation in amplitude, defined by a change in amplitude ΔA, a frequency ω and a phase ϕ, could be an interesting addition for an improved model.

Influence of environment　It can be observed in Figure 10a and Figure 10b that the values for 10 s are higher than the values for 5 s. This is due to the fact that many stars saturate the sensor for a sufficiently long exposure time. A trend seems to be emerging among these points: the average does not seem to depend on altitude. But many points do not respect this trend. The improved calculation, shown in Appendix F, gives smaller mean values that are more realistic because they are closer to the value found using ASTAP. ASTAP is not usable for the mean calculation because the cursor would need to be manually moved over all the stars, report the values and then average them. This would take a phenomenal amount of time. For small angles, the FWHM remains too high, due to the fact that the stars do not emerge sufficiently from the noise. In fact, the automatic calculation doesn't detect enough stars to find a coherent result. The problem is certainly the code used, which should be improved. Table 1 shows that the exposure time is not a parameter that reduces the ability to detect a satellite. Indeed, the magnitude of a Starlink's darksat is 6.6 which is brighter than the limiting magnitude for 0.5 s [8]. However, it is important to mention that the magnitude of a satellite is clearly reduced on an image. Indeed, light rays from a star strike the same pixels over time. As the telescope mount is calibrated to follow the rotation of the earth, the satellites leave a trace.

As a result, the light reflected by the satellite and captured by the satellite is spread out along the track. As a result, the satellite appears much less bright. Nevertheless, if the tracking was made to follow the satellite, the satellite's magnitude would be twice as large as the limiting magnitude. As expected, the limiting magnitude increases with time exposure. A quantitative study with other telescopes has been carried out and can be found in Appendix D.

Light pollution caused by cities such as Lausanne and Evian is clearly visible in the Figures 11a and 11b. Indeed, the magnitude of the faintest stars in pictures taken on the EPFL campus is smaller than the one taken at Astroval. The difference is almost 15 %. This phenomenum is also observable in table 1 for time exposure of 0.02 s. The measurement taken on the EPFL campus wasn't usable while the one at Astroval was.

Figures 12a and 12b show the influence of sky clarity. These results confirm that satellite detection can be done in the sporadic presence of clouds. Although significantly reducing the performance of the telescope, the satellites remain detectable. The reduction is about 15%. The presence of clouds means that altitude does not play an important role. Indeed, a limit of 18.7 mag for 10 s seems uncrossable.

Figures 13a and 13b show the influence of temperature and wind. The only differences between the two nights of observation were the temperature and the presence of wind. As already mentioned, the wind has certainly corrupted at least one of the measurements. The rest of the measure seems to be corrupted by the wind as well. Indeed, because the temperature is higher, the limiting magnitude is expected to be reduced. However, the opposite can be observed. Nevertheless, it can be concluded that even in the presence of wind, satellites are detectable with the telescope. To really observe the influence of temperature, more experiments should be done, although it is difficult to calculate the influence of the earth's temperature at ground level because the temperature of the upper layers of the atmosphere also is expected to play a major role.

Simulation As expected, the error using the Runge-Kutta 4 algorithm have a slope of approximately 4 and the convergence of Störmer-Verlet has a slope of 2. Fewer steps are needed to achieve satisfactory accuracy with Runge-Kutta. This justifies its use and the subsequent abandonment of Störmer-Verlet. In Figure 14a, there exists a minimum for $\Delta t = 4$ minutes followed by a plateau. The plateau appears because of the accumulation of errors on each steps. The minimum corresponds to the time interval that NASA uses to calculate the trajectory of the International Space Station (ISS) [7]. Moreover, the revolution time of the simulated satellite is 5579.995 s. This result is 4.155 s longer compared to the ISS revolution value which is 5575.84 s [9]. Without any perturbations implemented, the relative error is 0.072% on the revolution time.

The orders of magnitude of the point like Earth gravitation ($\sim 10^1$ m/s^2), the correction due to 3D Earth model ($\sim 10^{-2}$ m/s^2), the Moon gravitation ($\sim 10^{-6}$ m/s^2), the Sun gravitation ($\sim 10^{-6}$ m/s^2) match the values presented in the literature for altitudes of 400 km and 1000 km [10]. The solar radiation pressure order of magnitude ($\sim 10^{-9}$ m/s^2) doesn't match the value given in the literature($\sim 10^{-7}$ m/s^2). This can be partially due to the fact that the area facing the sun might be hard to determine since the orientation of the satellite changes over time. The drag force at 400 km is $\sim 10^3$ times bigger than at 1000 km which is expected since the air density ρ depends exponentially on the altitude. Figure 15a illustrates the need for additional forces or implementation correction since the simulated satellite ends up 35 km lower than the ISS in a day. By considering the order $k = 2$, the satellite reaches $r = 6200$ km which is below the Earth surface. Such phenomenon is clearly not realistic and can come from different parts of the implementation process. Further investigation should be done to fix the correction of the 3D earth gravitational potential.

8 Conclusion

The results obtained during the semester project has been useful in the development of the SSA EPFL association. Firstly, the aberrations have been removed using the bias frame, dark frame and flat field frame have been studied. All these artefacts were analysed to calibrate the images. Without this, it is impossible to clearly define the presence or absence of stars. This leads to the use of the Point Spread Function. The PSF is a crucial tool to analyse satellite tracks. Then, the influence of the environment has been studied. It has be shown that the light pollution between Lausanne and Jura's mountain has an impact of 15% on the limiting magnitude. This is equivalent to the presence of a cloud veil in the line of sight. The limits of the telescope have been studied. It was observed that the noise was too high for 0.02 s time exposures on campus. Therefore, it is impossible to analyse this kind of image. The next step would be to add complexity to the track model, such as taking into account the intrinsic rotation of the satellite. This effect causes a variation in track width as well as a variation in brightness. Another idea would be to study the performances of the telescope depending on the temperature of several atmospheric layers.

References

[1] European Space Agency, Space debris by the numbers, visited on 10.11.2021
https://www.esa.int/Safety_Security/Space_Debris/Space_debris_by_the_numbers

[2] Understanding Read Noise in sCMOS Cameras, Oxford Instruments, last visited on 28.05.2022,
https://andor.oxinst.com/learning/view/article/understanding-read-noise-in-scmos-cameras

[3] Flat fielding, Department of Physics, Durham University, last visited on 29.05.2022,
https://community.dur.ac.uk/physics.astrolab/flat_fielding.html

[4] Convolution, Wikipedia, last visited on 28.05.2022,
https://en.wikipedia.org/wiki/Convolution

[5] ASTAP, the Astrometric STAcking Program, last visited on 29.05.2022,
https://www.hnsky.org/astap.html

[6] Météo Suisse, last visited on 28.05.2022
https://www.meteosuisse.admin.ch/home/valeurs-mesurees.html?param=messwerte-lufttemperatur-10min&station=PUY&chart=day

[7] ISS Trajectory DATA, Nasa website, last visited on 31.05.2022 https://spotthestation.nasa.gov/trajectory_data.cfm

[8] First observations and magnitude measurement of Starlink's Darksat, J.Tregloan-Reed and al, March 2020

[9] Wolfram Alpha, last visited on 22.05.2022
www.wolframalpha.com

[10] Satellite Orbit by Oliver Montenbruck and Gill Eberhard, 2011

[11] 36 cm Rowe-Ackermann Schmidt Astrograph (RASA 36) Optical Tube Assembly (CGE Dovetail), Celestron, last visited on 25.05.2022,
https://www.celestron.com/products/36-cm-rowe-ackermann-schmidt-astrograph-rasa-36-optical-tube-assembly-cge-dovetail#specifications

[12] Dos and don'ts of reduced chi-squared, R. André, T. Schulze-Hartung & P. Melchior, 2010,
https://arxiv.org/pdf/1012.3754.pdf

[13] Autocorrelation analysis & convergence, emcee documentation, last visited on 31.05.2022,
https://emcee.readthedocs.io/en/stable/tutorials/autocorr/

[14] Characteristics of TELESTO, University of Geneva, last visited on 11.05.2022
https://plone.unige.ch/astrodome/telesto/manuels/characteristics-of-telesto

[15] ProLine PL16803 manual, University of Geneva, last visited on 11.05.2022
https://plone.unige.ch/astrodome/telesto/manuels/manuels/pl16803.pdf

[16] The VLT Survey Telescope ATLAS, T.Shanks and al, 20 February 2015

[17] An Overwiew of Reference Frames and Coordonate Systems in the SPICE Context, Navigation and Ancillary Information Facility (NAIF), January 2020
https://naif.jpl.nasa.gov/pub/naif/toolkit_docs/Tutorials/pdf/individual_docs/17_frames_and_coordinate_systems.pdf

[18] PHYSIQUE NUMERIQUE I-II by Prof. Laurent Villard, September 2020

A Telescope characteristics

The telescope is a Celestron Rowe-Ackermann Schmidt Astrograph 36 cm [11]. The telescope consists of a main mirror 35.5 cm in diameter, reflecting the light to a set of lenses in front. This set of lenses is responsible for focusing the light onto the camera sensor, which is also situated in front of the camera. The central obstruction diameter is 158 mm. The focal length is 795 mm. The aperture is therefore $f/2.2$, which is considered extremely luminous. According to the constructor, the angular resolution is 0.39".

The mount is a Celestron CGX-L with *go-to* and sky tracking capabilities. This means having the possibility to indicate a given point in space for the mount to point to and the mount automatically compensating the earth's rotation.

The camera is a ZWO ASI 2600 MM Pro monochrome. The 23.5×15.7 mm^2 sensor has a resolution of (6248×4176) pixels. The full well capacity is $50'000$ electrons whereas the read-out noise is between 1 and 3 electrons. The quantum efficiency is 91%. The pixel values are recorded in 16 bits, i.e. between 0 and 65535. In order to avoid increased thermal noise during long exposures, the camera can be cooled

Figure 16: Picture of the telescope on the EPFL campus.

using the Peltier effect. Combined with the telescope, this camera gives a field of view of 1.14°×1.71°, which is approximately twice the angular size of the full moon. The angular resolution is therefore 0.72".
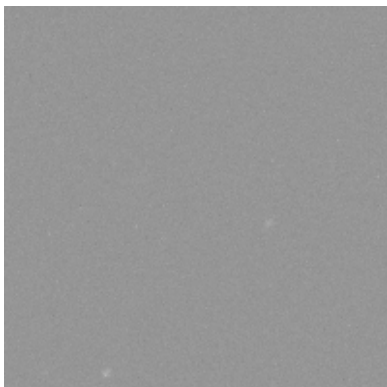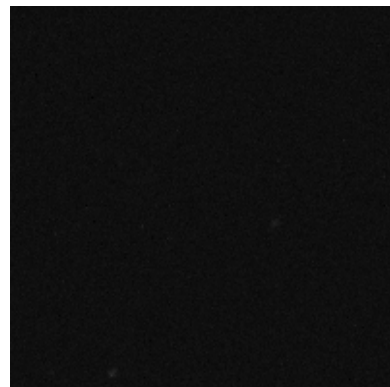
B Calibration

B.1 Readout noise

A part of the raw image is shown on Figure 17a and the same part of the calibrated image is shown on Figure 17b. The background is, after calibration, properly black.

(a)

(b)

Figure 17: 100 by 100 pixels outcut of a raw image (a) and after removing the bias frame (b).

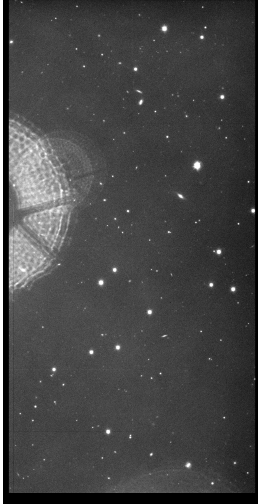### B.2 Internal reflection: the need for flatfielding in the VST

Figure 18: Part of the image showing an internal reflection of the secondary mirror for the VST.

As Figure 18 shows, there is a reflection of the secondary mirror (bright spot on the left). This reflection is visible in all images, including in images taken during the time between the sunset and the apparition of the first stars. Such images will be perfectly uniform in luminosity (hence the name *flat frames*) except for those kind of imperfections. Therefore, one can remove the imperfections by dividing the image of interest by the (normalised) flat frame. The raw images from VST were very kindly provided by LASTRO laboratory PhD student E. Rachith.

B.3 Uneven angular resolution

In order to estimate the size of the smallest object measurable, one has to know the FWHM of a point source (i.e. a star) on the part of the sensor. This is obtained by detecting every star on the image, fitting a 2D Gaussian distribution on every star and measuring the FWHM of each fit. For further discussion, see Chapter 4.1

By using multiple images, where the stars are not in the same area of the camera sensor, one can fill out the map of the FWHM across the whole sensor. This is represented in Figure 19. Since the measurement is focused on the smallest detail possible, the largest stars present in each image were not considered. The result was obtained using 39 images and around 200 stars per image. To fill out the empty areas between the different measurements, the nearest value interpolation was performed on the image.
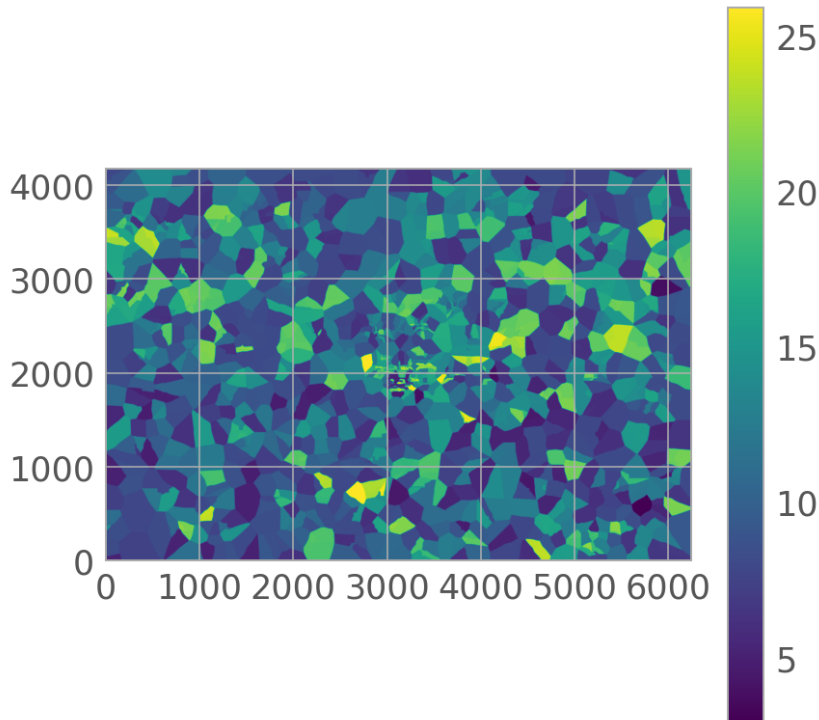

Figure 19: FWHM across the whole sensor using 39 images, with around 200 point like sources per image. The interpolation between measurement was done using the nearest value.

C   Forward modelling

In order to find the model parameters that give the correct track once convolved with the PSF, a likelihood maximisation algorithm has been used. In order to measure the goodness of the model, a reduced chi-square test has been used on the pixels containing the track[5]. The reduced chi-square formula is given by

$$\chi^2_{red} = \frac{1}{N} \sum_n^N \frac{(y_n - M(x_n, \theta))^2}{\sigma_n^2}, \tag{4}$$

where N is the number of pixels, y_n are the measured luminosity of each pixel, $M(x_n, \theta)$ is the function describing the model, x_n the index of each pixel and σ_n the uncertainty on each pixel [12]. The uncertainty used in the following computations are the standard deviation of the background noise denoted σ. The matrix representing the outcut has been mapped to a long one-dimensional vector. The log-likelihood $\ell_l(\theta)$ of the model given a parameter θ is then given by $\ell_l(\theta) = -0.5 * \chi^2_{red}(\theta)$.

The log probability of this model is then $\ell(\theta) = \ell_l(\theta) + \ell_p(\theta)$, where $\ell_p(\theta)$ is the prior log-likelihood. This function can be used to weight the probabilities of different parameters based on prior knowledge of the reality modelled. In this report, the prior log-likelihood is used to limit the scope of the parameters to coherent values, such as i_0 and i_{end} coordinates inside the outcut, a width $w < 20$ pixels and an amplitude $A < 10^5$ [6]. The prior log probability is uniformly distributed for the coherent values.

The algorithm selected to find the optimal parameters is an affine invariant Markov chain Monte Carlo ensemble sampler. This algorithm allows to optimise θ and find the confidence interval for each parameter. To verify that the algorithm is working well, it has been tested on a fake track created manually on which random noise has been added. The noise followed a normal distribution with the same mean value and standard deviation as the background noise in the real images. The explorations of the parameter space are done by so-called *walkers*, which trajectory is randomly generated step by step with probabilities given by the log probability. Their trajectories are shown in Figure 20a. By counting the number of occurrences of each parameter, one can find the distribution of each parameter. This is shown on Figure 20b. Such as Figure is called a corner plot. The distribution of each parameter is the histogram, whereas the 2D plots represent the inter-effects of two different parameters.

The number of walkers can be manually varied to give more or less data points (at the cost of more or less computation time). The number of iterations can be manually varied, but must be higher than 50 times the auto-correlation time ξ in order to be assured that the parameter space has been properly sampled [13]. More iterations than 50ξ do not lead to better results.

A fit on the distribution of each parameter is computed in order to find the value of the highest likelihood and the confidence interval. In practice, the average value and the standard deviation have been computed. This method is coherent with the distributions for the starting coordinates and the amplitude i_0, i_{end} and A, but not for the width w. The difference between the track obtained from the real parameters and the track obtained from the mean values is shown in Figure 21a. The colour indices are represented as a function of the standard deviation of the background noise σ.

---

[5]This means neglecting the background pixels around the track.

[6]The maximal width has been selected as it would represent an object of 40 m in diameter, which is the case for the very few largest objects in orbit. The amplitude has been limited to 10^5 because no brighter track has been detected during the measurements.
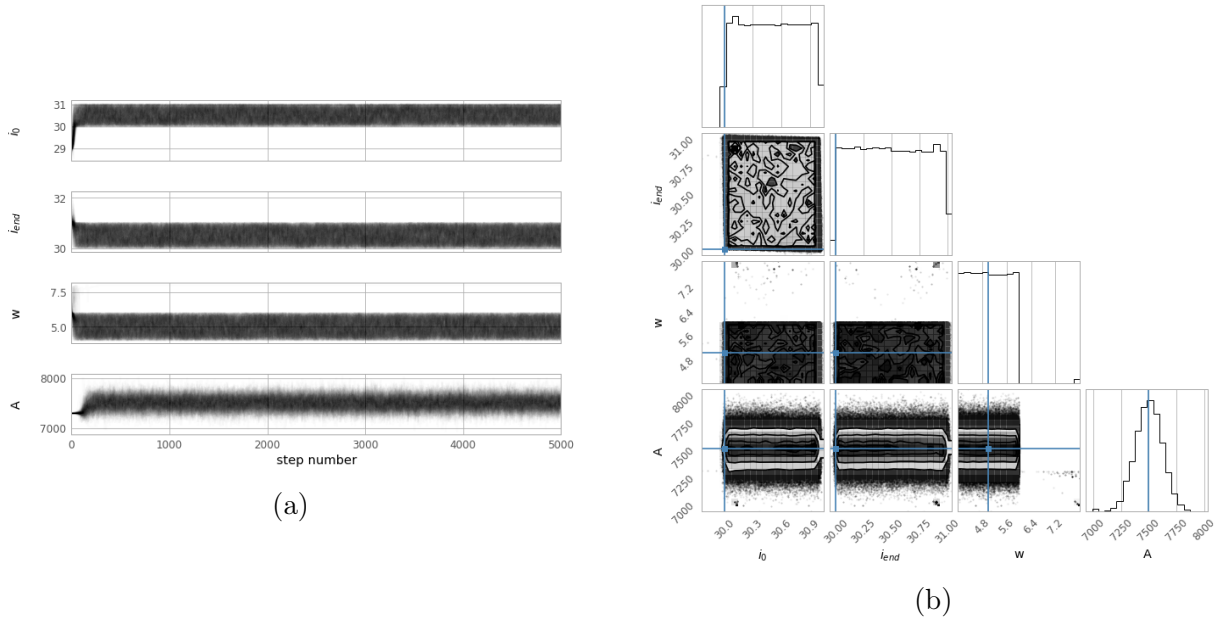
(a)

(b)

Figure 20: The trajectory of all walkers during the Monte-Carlo simulation (a) and the corner plot of the parameters (b). The blue lines represent the actual values. The real parameters where $\theta = (30, 30, 5, 7500)$ and the solutions were $\theta = (3(0.5 \pm 0.3), (30.5 \pm 0.3), (5.0 \pm 1), (7500 \pm 100))$. The solution has reduced a chi-squared value of $\chi^2_{red} = 1.3$. It represents a signal to noise ratio of SNR = 122.
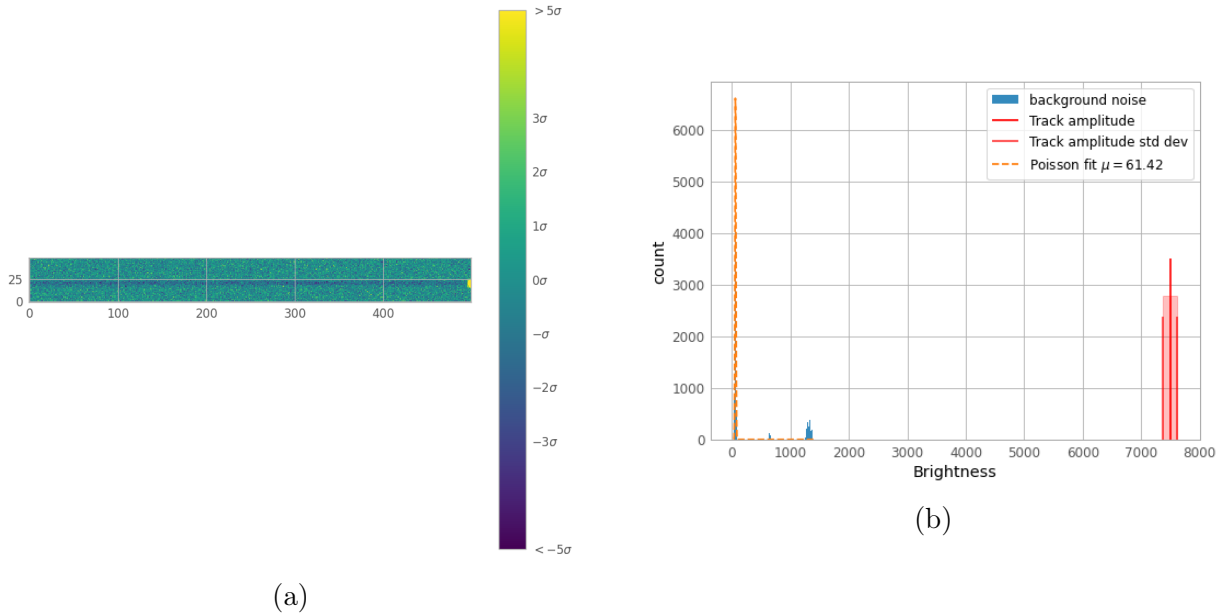

(a)

(b)

Figure 21: The difference between the real track model and the solution found using Monte-Carlo simulation (a) and the background distribution with the amplitude found using Monte-Carlo simulation (b). The real parameters where $\theta = (30, 30, 5, 7500)$ and the solutions were $\theta = (3(0.5 \pm 0.3), (30.5 \pm 0.3), (5.0 \pm 1), (7500 \pm 100))$. The solution has reduced a chi-squared value of $\chi^2_{red} = 1.3$. It represents a signal to noise ratio of SNR = 122.

D   Comparison with other telescopes

D.1   TELESTO

The official telescope of the LASTRO laboratory at EPFL is called TELESTO in the AS-TRODOM observatory in Sauvergny, Switzerland[7]. Its primary mirror is 60 cm in diameter and its focal range is 2280 mm. The attached CCD camera is a monochrome water cooled ProLine PL16803 with a resolution of 4096×4096 pixels. The full well capacity is $100'000$ electrons. This setup gives a field of view of 0.9 °×0.9 ° [14][15].

Using images captured by two PhD students in the LASTRO laboratory[8], the limiting magnitude has been measured using the same process as outlined in Chapter 5. The images received consisted of 15 s exposures as well as 30 s exposures. Calibration frames were also provided (namely one dark frame per exposure time and seven bias frames). The images were taken 35° above the horizon. The measured limiting magnitude for 15 s exposures is $m_l = (15 \pm 1)$ mag and the measured limiting magnitude for 30 s exposures is $m_l = (16.8 \pm 0.3)$ mag. The angular resolution is found to be about 4". Comparing by taking images with the same altitude for 30 s using LOST, the limiting magnitude is (18.6 ± 0.1) mag.

Based on this measurement, the LOST prototype is capable of detecting fainter stars, because of its larger aperture. While the field of view is slightly smaller for TELESTO compared to LOST, the angular resolution is comparable. This means that the wider field of view obtained using LOST increases the likelihood to observe a satellite or debris without any loss in precision.

D.2   VST

The ATLAS survey perform its activity on the VLT Survey Telescope (VST). The telescope is located in Chile. The diameter of the main mirror is 2.61 meters. There are 32 CCD camera with 4000x2000 pixels. Each pixel has a size of 0.21". Therefore, the field of view is $1° \times 1°$ [16]. The limiting magnitude found for an airmass of 1.3 is 22.67. This measurement is taken with a red filter. The limit is calculated for a SNR bigger or equal to 5. The exposure time is 2×45 s. This value is 18% better than that obtained with LOST by taking a 3×30 s image. The value taken with the LOST prototype is (18.7 ± 0.5) mag. Nevertheless, this value is calculated with limit value of SNR bigger or equal to 7.

E   Simulations

E.1   The referential

In order to compute the trajectory, the J2000 reference frame has been chosen. This system is geocentric and the axes are static with respect to the earth intrinsic rotation. The z-axis is taken along the Earth north pole, the x-axis in the direction of the vernal equinox and the y-axis is then defined by the right-hand rule. The intersection of the ecliptic and the equatorial plane defines a line. The vernal equinox is defined by the side of the line which is given by the ascending node. Because of the movement of precession and nutation of the earth, the equatorial plane varies, implying that the vernal equinox is not fixed, hence the necessity to choose its position at a specific time. In the J2000 frame, the chosen epoch is the first of January 2000. A scheme in Figure 22 allows to visualise the reference frame.

---

[7]The observatory is a joint facility between the University of Geneva and EPFL

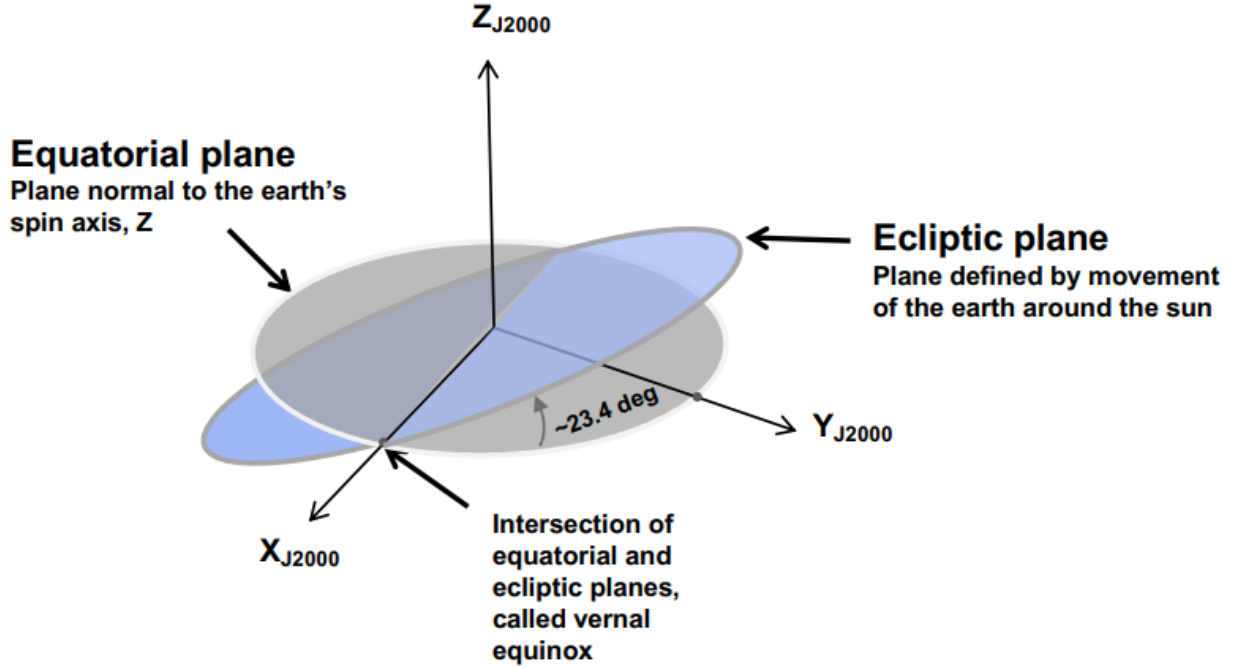[8]Belén Yu Irureta-Goyena and Elisabeth Rachith

Figure 22: Scheme of the J2000 referential frame and coordinate system [17].

E.2 Forces

Different forces have been implemented by descending order of magnitude. The importance of the forces varies with the altitude of the object considered. The altitudes considered to classify the order of magnitude will be 400 km, which corresponds roughly to the ISS orbit, and 1000 km. This ranking is given in *Satellite Orbit* by O. Montenbruck and E. Gille [10].

E.2.1 Gravitation of Earth as a point like mass

As a first approximation, the Earth is considered as a point like mass. The acceleration provoked is then simply given by

$$\ddot{\mathbf{r}} = -\frac{GM_E}{r^3}\mathbf{r}, \tag{5}$$

where G is the gravitational constant, M_E is the mass of the Earth and $\mathbf{r}$ is the position vector of the object.

E.2.2 Geopotential of the earth

By considering the earth as a 3D object with non-homogeneous mass density, this should gives rise to an additional acceleration of 10^{-5} km/s^2 in norm [10]. The potential U is defined by

$$U = G \int \frac{\rho(\mathbf{s})d^3\mathbf{s}}{|\mathbf{r} - \mathbf{s}|}, \tag{6}$$

where $\rho(\mathbf{r})$ is the mass density distribution of the Earth. The potential U is linked to the acceleration by the relation

$$\ddot{\mathbf{r}} = \nabla U. \tag{7}$$

After expanding in spherical harmonics the right hand side of the equation (6) and a few operations, the calculation leads to the formula

$$U = \frac{GM_E}{r} \sum_{n=0}^{\infty} \sum_{m=0}^{n} \frac{R_E{}^n}{r^n} P_{nm}(\sin\phi)(C_{nm}\cos(m\lambda) + S_{nm}\sin(m\lambda)), \tag{8}$$

where R_E is the Earth radius, r is the norm of $\mathbf{r}$, P_{nm} are the associated Legendre polynomials, ϕ is the declination and λ the right ascension in the equatorial system of coordinates and the C_{nm} and S_{nm} are empirical coefficients linked to the mass density distribution of the Earth $\rho(\mathbf{r})$. In the equation (8), there's a sum over an infinite amount of term. In practice, only $k+1$ terms will be considered. Note that for $k = 0$, the equation gives back the results found for the point like mass Earth computed in equation (5) since $P_{00}(x) = 1$, $C_{00} = 1$ and $S_{00} = 0$.

E.2.3   Atmospheric Drag

The acceleration due the atmospheric drag can be written by

$$\ddot{\mathbf{r}} = -\frac{1}{2}C_d\frac{A}{m}\rho(\mathbf{r})v_r^2\mathbf{e_v}, \tag{9}$$

where C_d is the dimensionless drag coefficient, A is the cross-sectional area of the satellite, m is the mass of the satellite, $\rho(\mathbf{r})$ is the density of the atmosphere, v_r is the velocity of the object relatively to the atmosphere and $\mathbf{e_v}$ is the unit vector giving the direction of the satellite. The equation to compute v_r is given by

$$\mathbf{v_r} = \mathbf{v} - \omega_{\mathbf{E}} \times \mathbf{r}, \tag{10}$$

where $\mathbf{v}$ is the velocity of the satellite and $\omega_{\mathbf{E}}$ is the angular velocity of the Earth, which we will consider here as equivalent to the angular velocity of the atmosphere. To describe the atmospheric density $\rho(\mathbf{r})$, many different empirical models are possible. The drag force depends highly on the altitude of the satellite. The Harris-Priester model gives values of $\rho(\mathbf{r})$ for altitudes from 100 km to 1000 km. This model seems well suited since below 100 km the objects would drop because of the high atmosphere density. Above 1000 km, the atmosphere density is sufficiently small that the drag force becomes negligible. In addition, this model takes in consideration the fact that the sun's radiations tends to increase the atmosphere's density.

E.2.4   Gravitation of the Moon and the Sun

Since the Sun and the Moon are far away from the satellite, they will be considered as point like masses. By Newton's law of gravity, the acceleration is given by

$$\ddot{\mathbf{r}} = GM\frac{\mathbf{s} - \mathbf{r}}{|\mathbf{s} - \mathbf{r}|^3}, \tag{11}$$

where M is the mass of the Sun or the Moon and $\mathbf{s}$ is the position of the Sun or the Moon. But since the referential frame chosen is non-inertial, the acceleration of the Earth provoked by the Sun or the Moon has to be subtracted which leads to the equation

$$\ddot{\mathbf{r}} = GM\left(\frac{\mathbf{s} - \mathbf{r}}{|\mathbf{s} - \mathbf{r}|^3} - \frac{\mathbf{s}}{|\mathbf{s}|^3}\right). \tag{12}$$

E.2.5 Solar radiation pressure

The acceleration caused by the solar radiation pressure close to the earth can be computed according to the following relation

$$\ddot{\mathbf{r}} = \frac{\sigma T^4}{\pi c} \left(\frac{R^2}{L^2} \right) \frac{A}{m}, \tag{13}$$

where σ is the Stefan-Boltzmann constant, T is the temperature of the Sun at its surface, c is the speed of light, R is the radius of the Sun, L is the Earth-Sun distance, A is the surface of the satellite exposed to the Sun radiation and m is the mass of the satellite.

E.3 Detailed Computations of Table 2

To compute the values presented in Table 2, some considerations needed to be done except for the point like Earth gravitation and the solar radiation pressure. The parameters used for the simulation are presented in Table 3.

Sun's Mass	1.989×10^{30} kg
Moon's Mass	7.35×10^{22} kg
Earth's Mass	5.97×10^{24} kg
Distance Earth-Moon	3.84×10^{8} m
Distance Earth-Sun	1.49×10^{11} m
Earth's Radius	6.37×10^{6} m
Sun's Radius	6.957×10^{8} m
Air Density Min (400 km)	2.249×10^{-12} kg/m^3
Air Density Max (400 km)	7.492×10^{-12} kg/m^3
Air Density Min (1000 km)	1.15×10^{-15} kg/m^3
Air Density Max (1000 km)	1.81×10^{-14} kg/m^3
Earth's Intrinsic Angular Velocity	7.292×10^{-5} m^{-1}
Sun's Temperature	5778 K
Gravitational constant	6.67×10^{-11} Nm^{2}kg^{-2}
Speed Of Light	$299'792'458$ ms^{-1}
Stefan-Boltzmann Constant	5.670374×10^{-8} Wm^{-2}K^{-4}
Satellite's Velocity	8×10^{3} m/s
Satellite's Drag Coefficient	3
Satellite's Area Mass Ratio	3×10^{-3} kg/m^2

Table 3: Values used to compute the results of Table 2. The air densities are given in the literature [10]

E.3.1 3D Earth Gravitation

For the Earth gravitation, the equation (5) has been used for the point like model and equations (7) and (8) with $k = 2$ for the 3D Earth gravitation.

E.3.2 Sun's and Moon's Gravitation

For the gravitation of the Sun (respectively the Moon), the situation where the Earth, the satellite and the Sun (Moon) are aligned is considered. With such consideration and using

equation (12), the norm of the acceleration becomes

$$\ddot{r} = GM\frac{2sr + r^2}{s^2(s + r)^2},\tag{14}$$

where M is either the mass of the Sun or the Moon.

E.3.3 Atmospheric Drag

The maximum atmospheric drag for a given velocity is reached in the case where the satellite goes in the opposite direction of the Earth rotation and when the solar radiations are at their strongest. The minimum is reached when the satellite goes in the same direction as the Earth rotation and without solar radiation. The satellite position is considered with latitude 0. The results are computed with those considerations applied to equation (9).

E.4 The numerical integration

E.4.1 Runge-Kutta 4

In this section, the equation for the numerical integration of Runge-Kutta 4 are [18]

$$\begin{cases} \mathbf{k_1} = \Delta t \mathbf{f}(\mathbf{y_i}, t_i), \\ \mathbf{k_2} = \Delta t \mathbf{f}(\mathbf{y_i} + \frac{1}{2}\mathbf{k_1}, t_{i+1/2}), \\ \mathbf{k_3} = \Delta t \mathbf{f}(\mathbf{y_i} + \frac{1}{2}\mathbf{k_2}, t_{i+1/2}), \\ \mathbf{k_4} = \Delta t \mathbf{f}(\mathbf{y_i} + \mathbf{k_3}, t_{i+1}), \\ \mathbf{y}_{i+1} = \mathbf{y}_i + \frac{1}{6}[\mathbf{k_1} + 2\mathbf{k_2} + 2\mathbf{k_3} + \mathbf{k_4}], \end{cases}$$

$\mathbf{y}_{i+1}$ is the position (respectively the velocity) at the step $i + 1$ and $\mathbf{f}(\mathbf{y_i})$ is the velocity (respectively the acceleration) as a function of $\mathbf{y_i}$.

E.4.2 Stormer-Verlet

In this section, the equations for the numerical integration of Störmer-Verlet are [18]

$$\begin{cases} \mathbf{q}(t + \Delta t) = \mathbf{q}(t) + (\Delta t/m)\mathbf{p}(t) + ((\Delta t)^2/2m)\mathbf{F}(\mathbf{q}(t)), \\ \mathbf{p}(t + \Delta t) = \mathbf{p}(t) + (\Delta t/2)[\mathbf{F}(\mathbf{q}(t + \Delta t)) + \mathbf{F}(\mathbf{q}(t))], \end{cases}$$

$\mathbf{q}(t)$ is the position of the satellite at time t, $\mathbf{p}(t)$ is the momentum of the satellite at time t and $\mathbf{F}(\mathbf{q}(t))$ is the acceleration of the satellite as a function of the position at time t.

F Influence of environment: additional Figure

Figure 23a and Figure 23b show the FWHM of the 2D-Gaussian PSF. Theses sets of measurements were taken during two different night on the EPFL campus for time exposure of 0.5 s and 10 s. Figure 24 show the FWHM of the 2D-Gaussian PSF. Theses sets of measurements were taken at Astroval for time exposure of 0.5 s and 10 s. This value are found using the other technique.
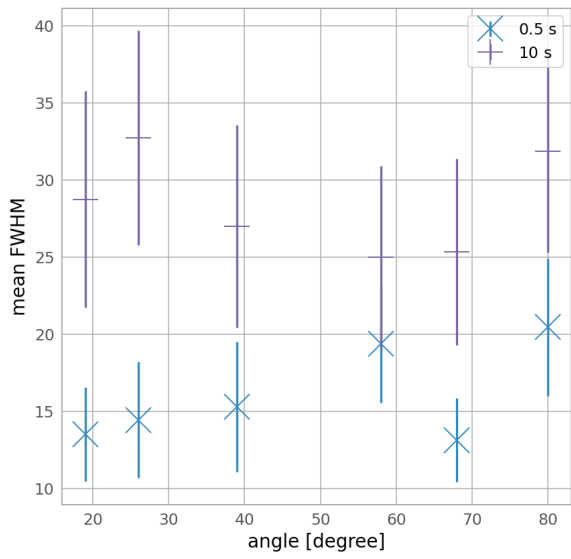
(a)
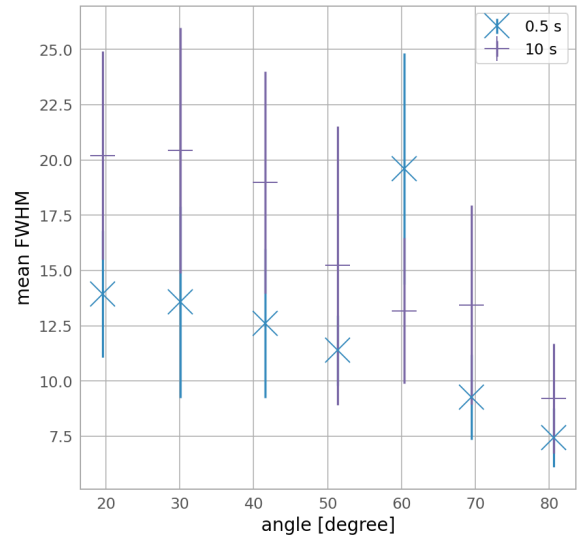
(b)

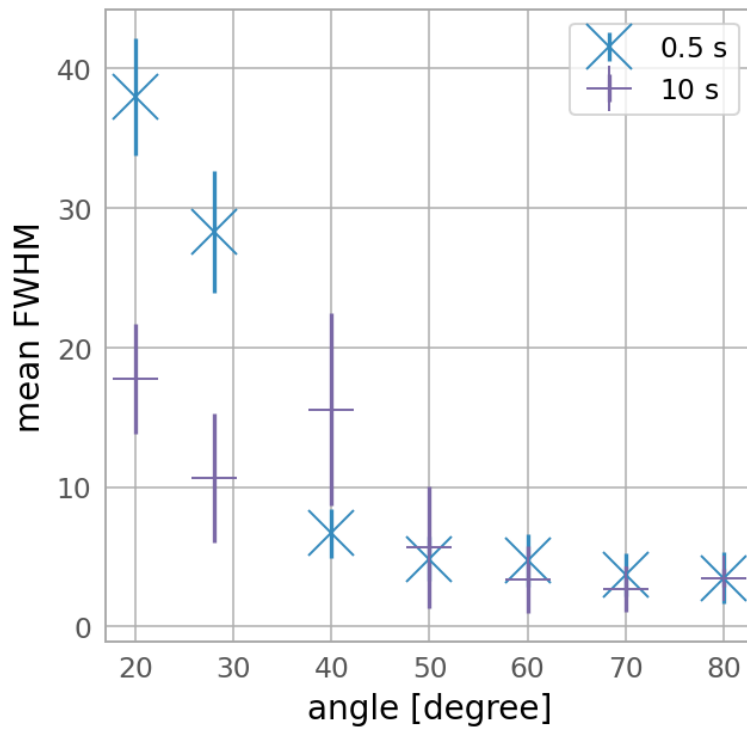Figure 23: FWHM on campus the first night (a) and second night (b) as a function of the altitude.

Figure 24: FWHM on campus as a function of the altitude. The FWHM is calculated using the technique proposed by Prof. Kneib.